Ternary Metal Chalcogenide Heterostructure (AgInS$_2$−TiO$_2$) Nanocomposites for Visible Light Photocatalytic Applications

Priyanka Ganguly,[†,‡] Snehamol Mathew,[†,‡] Laura Clarizia,[‖] Syam Kumar R,[§] Akinlolu Akande,[§] Steven J. Hinder,[⊥] Ailish Breen,[†,‡] and Suresh C. Pillai*[,†,‡]

[†]Nanotechnology and Bio-Engineering Research Group, Department of Environmental Science, [‡]Centre for Precision Engineering, Materials and Manufacturing Research (PEM), and [§]Mathematical Modelling Research Group, Department of Health and Nutritional Sciences, Institute of Technology Sligo, F91 YW50 Sligo, Ireland

[‖]Dipartimento di Ingegneria Chimica, dei Materiali e della Produzione Industriale, Università di Napoli Federico II, p. le V. Tecchio 80, 80125 Napoli, Italia

[⊥]The Surface Analysis Laboratory, Faculty of Engineering and Physical Sciences, University of Surrey, GU2 7XH Guildford, Surrey, United Kingdom

S *Supporting Information*

ABSTRACT: Hybrid nanoarchitectures of AgInS$_2$ and TiO$_2$ photocatalysts were prepared by using a modified sol−gel method. The experimental results reveal that these nanocomposites display enhanced visible light absorption and effective charge carrier separation compared to their pristine parent samples (AgInS$_2$ or TiO$_2$). 0.5 wt % AgInS$_2$ loading was found to be the optimum concentration for photocatalytic applications. More than 95% of doxycycline degradation was achieved within 180 min of solar light illumination. Similarly, the dopant concentrations at lower values (<2 wt %) exhibited 300 times higher H$_2$ generation rate under visible light irradiation compared to AgInS$_2$ and TiO$_2$. The microbial strains (*Escherichia coli* and *Staphylococcus aureus*) exhibited a 99.999% reduction within half an hour of simulated solar light illumination. The computational investigation was employed to understand the structural, electronic, and the dielectric properties of AgInS$_2$ and TiO$_2$ composites. The improved photocatalytic results are explained as a result of the decreased rate of exciton recombination. The current investigation opens up new insights into the use of novel ternary heterostructure nanocomposites for improved visible light activity.
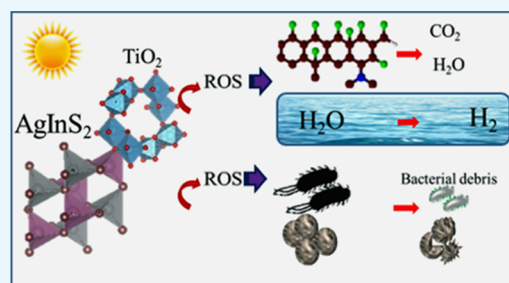
1. INTRODUCTION

Fossil fuels such as coal and natural gases have been the mainstay for the industrialized world for the past century.[1,2] However, their rapid depletion and ever-increasing demand raise some grave challenges.[3,4] Rising global temperature and population are the key elements of concern in relation to energy shortage and environmental pollution.[5,6] Hydrogen is considered as the fuel for the 21'st century.[7−9] However, processes such as steam reforming utilizing coal are still the major route to generate H$_2$.[10−13] Similarly, the water plants across different cities around the globe utilize the conventional route of adsorption, sedimentation, and flocculation as secondary water treatment protocols.[14,15] This results in the disposal of untreated hostile effluents to the ecosystem, which further leads to channelization to a higher order of the food chain via biomagnification.[16,17] The lack of cost-effective and sustainable technologies has been a challenge for this region.[14,15] Nevertheless, sustainable technologies such as solar and wind energy have emerged to be efficient alternatives for modern civilization.[18,19] Among the various sustainable technologies, photocatalysis is identified as one of the long-term, stable, environmentally friendly alternative, to produce

green energy and environmental remediation.[4,20−23] Semiconductor-based heterogeneous photocatalysis has the ability to utilize solar energy to convert and store into other renewable forms of energy, chemical fuels, degradation of harmful effluents, and even disinfection of microorganisms.[24−28] A photocatalytic process is defined by five basic steps: (1) Absorption of light on the semiconductor surface, (2) creation of photogenerated electron−hole pairs, (3) migration of these excitons or recombination, (4) adsorption of reactants and the desorption of the products, and (5) completion of redox reactions on the photocatalytic surface.[29−31] Thus, finding light-absorbing materials with semiconducting properties is not enough, but tailoring the design to effectively enhance the interfacial charge transfer and decreasing the rate of recombination is the key attribute. Various procedures such as band gap modulation, defect formation, dimensionality alteration, pore texture alteration, surface sensitization, heterojunction creation, etc. are attemp-

ted to reduce the recombination rate and enhance the visible light absorption.[24,29]

Titania is a traditional semiconductor material, which garnered significant attention in 1972 when Honda and Fujishima demonstrated its use in the electrochemical water splitting reaction to produce hydrogen.[32,33] Apart from the key properties, there exist major drawbacks such as low visible light absorption and wide band gap.[18,34,35] However, heterostructure formation of titania with other semiconductor materials has pushed them back into the spotlight. Ternary chalcogenides are another class of multicomponent elements, which have attracted attention for their small band gap and excellent photon absorption in the visible region of the electromagnetic spectrum.[25,36] These attractive multielement structures have been in the research realm for the past 3 decades, but their utilization as a possible heterostructure component for photocatalytic applications is still underexploited. Although copper-based ternary compounds have recently been explored for several photocatalytic applications such as degradation of emerging pollutants, real wastewater treatments, CO_2 reduction, and energy generation,[37−40] silver-based ternary compounds as a potential heterostructure component are yet to be studied and there exists enough opportunity to explore.

Amid all, $AgInS_2$(I-III-VI), a ternary semiconductor, crystallizes into two different polymorphs; a room-temperature stable tetragonal chalcopyrite structure and the other high-temperature orthorhombic wurtzite structure.[41] The phase transition occurs at 620 °C, and these nanocrystals are known to be synthesized using different liquid-phase reactions.[42−45] The orthorhombic $AgInS_2$ has been reported for various photocatalytic applications.[46] The small band gap and excellent photon absorption in the visible region of the electromagnetic spectrum aid in several efficient processes. Nevertheless, these materials display reduced quantum efficiency and strong light etching that confines its significant application.[47] Yin and Cui et al. reported the synthesis of $AgInS_2$ nanoparticle-sensitized TiO_2 nanotube arrays and $AgInS_2$ cluster films on the TiO_2/FTO substrate, respectively. These composites were investigated for their photoelectrochemical properties.[48,49] Similarly, Liu et al. effectively studied the same composite and illustrated the degradation of 1,2 dichlorobenzene.[47] Similar heterostructural composites such as $AgBiS_2$-TiO_2 were also previously reported.[50] However, there still exists significant potential of these materials for their various functional applications, which remains unexplored. Studies of these composites for photocatalytic hydrogen production, doxycycline (DC) degradation, and antibacterial disinfection have not yet been reported.

Hence, in the current investigation, we outline the optimal solvothermal synthesis parameters of $AgInS_2$ and developed a staggered heterostructure composite of TiO_2 at different wt % (0.5, 1, 2, and 5). These as-prepared composites illustrate positive heterostructure formation in the Raman and the X-ray photoelectron spectroscopy (XPS) results. Moreover, the UV−vis diffuse reflectance spectroscopy (UV-DRS) spectra illustrate the enhanced visible light absorption by the composite samples. The decreased band gap of the material enabled in illustrating 300 times enhanced hydrogen output, 5-log bacterial inactivation within 30 min of illumination, and more than 95% degradation of doxycycline (DC) within 3 h of irradiation. The introduction of even a low dopant ratio of $AgInS_2$ effectually harnessed the efficiency of the incoming light and decreased the recombination rate. A plausible photocatalytic mechanism and the interfacial charge transfer are discussed.

2. RESULTS AND DISCUSSION

2.1. Computational Results. In this section, computational results concerning the structural properties, the electronic structure, the projected density of states (PDOS), and dielectric properties of TiO_2 and $AgInS_2$ are presented. This helped to understand the underlying photocatalytic mechanism. The initial structures of TiO_2 and $AgInS_2$ were obtained from the Materials Project library. The initial geometry of $AgInS_2$ had the lattice constants $a = 6.81$ Å, $b = 7.15$ Å, $c = 8.35$ Å, and the angles were $\alpha = \beta = \gamma = 90°$. After the structural optimization, there were no changes in the lattice angles, but the lattice constants slightly changed upon volume relaxation to $a = 6.75$ Å, $b = 7.05$ Å, and $c = 8.25$ Å. The volume was relaxed by 3.5% in the case of orthorhombic $AgInS_2$. The X-ray diffractogram (XRD) pattern of the orthorhombic phase of $AgInS_2$ obtained theoretically is also given in Figure S1. Both the Ag and In cations have tetrahedral coordination with S. The AgS_4 and InS_4 tetrahedra are connected to one another at the corners (see polygons diagrams in Figure 1).
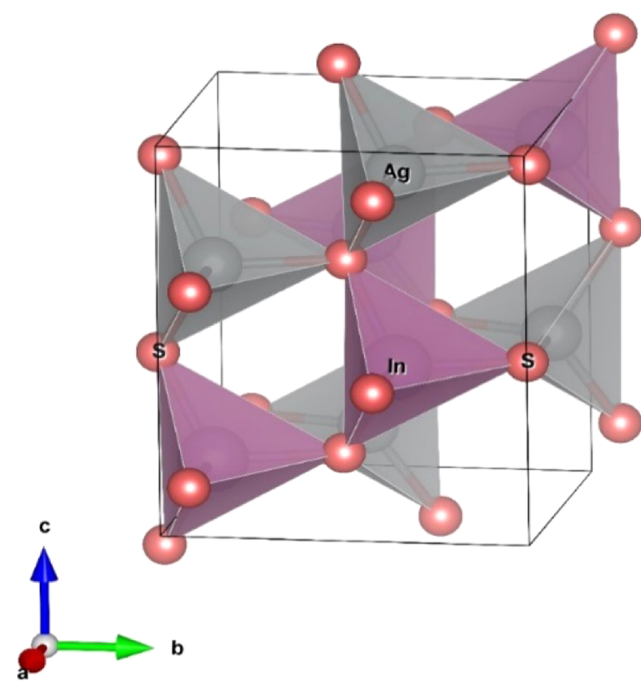

Figure 1. (Color Online) Optimized crystal structure of $AgInS_2$. Color code: gray = Ag, light red = In, and red = S.

TiO_2, on the other hand, had lattice constants $a = b = 10.16$ Å and $c = 2.96$ Å and the lattice angles $\alpha = \beta = \gamma = 90°$ at the end of the geometry relaxation where the volume was reduced by 3.77% from the initial structure. The initial structure of TiO_2 had the lattice parameters $a = b = 10.32$ Å and $c = 2.98$ Å and angles $\alpha = \beta = \gamma = 90°$. The Ti cations and O anions are connected to each other in an octahedral coordination. Alternate edge and corner sharing connect these octahedra to each other, as seen in Figure 2.

There is an underestimation in the band gap value with respect to the experimentally observed value even though the computed lattice parameters fall within a 1% error with respect
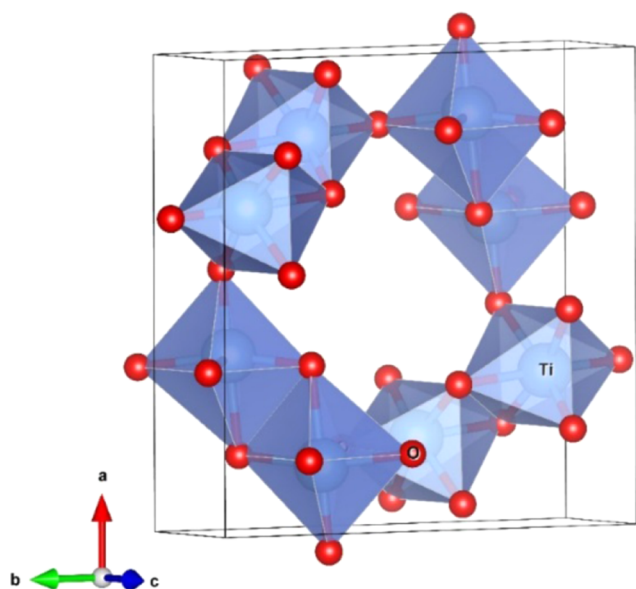
Figure 2. (Color Online) Crystal structure of TiO_2 in the tetragonal phase. Color code: blue = Ti and red = O.

to the experimental ones. This is not unexpected as the generalized gradient approximation (GGA) functional used is well-known to underestimate the band gap.[54] In the calculation of the band structure, the Perdew–Burke–Ernzerhof (PBE) functional under GGA was used owing to its computational speed. This functional is known to contain unphysical Coulomb repulsion, which leads to a poor description of the band gap.[51,52] There are works that report the PBE band gap of well-known compounds, which are shown to underestimate the experimentally observed band gap.[3] In fact, there are many insulators (nonzero band gap) such as FeO and GaSb that were estimated as metals (zero band gap) upon the usage of PBE functional.[53] The band structure of $AgInS_2$ is presented in Figure 3a and shows a direct band gap of ∼0.5 eV. Both the valence band maxima (VBM) and the conduction band minima (CBM) lie on the Γ point in the Brillouin zone. The upper valence band (UVB) is dominated by S p-orbitals and Ag d-orbitals and the lower conduction band (LCB) by the In s-orbitals and S p-orbitals. Energy larger than the computed band gap value is expected for the electrons to transfer from VB to CB due to the p–p forbidden transitions. In the current work, the experimentally observed band gap of $AgInS_2$ is 1.95

eV (Figure 11b), and the PBE band gap is 0.5 eV, which is within an error of 74.36%. The band structure and partial density of state (PDOS) plots were only used as a tool to illustrate the orbital occupancies near the band edges.

TiO_2, on the other hand, is an indirect band gap material with a band gap of ∼2.7 eV. The band structure and the PDOS of TiO_2 are shown in Figure 3b. The VBM lie between Z and P points, and the CBM lie between the Γ and X points of the Brillouin zone. The O p-states dominate the UVB, and the Ti d-states dominate the LCB. The Ti p-states were also present at the UVB of TiO_2.

Absorption spectra for $AgInS_2$ and TiO_2 are calculated in the independent particle approximation and plotted in Figure 4 in the range of 0−7.5 eV input light. The first peak of the imaginary part of the dielectric function, which indicates the energy value at which the actual electron transition starts, of $AgInS_2$ and TiO_2, was found to be 2.04 and 3.43 eV, respectively.[55] $AgInS_2$ is optically anisotropic, but along the x- and y-directions, the light absorption spectrum is isotropic for TiO_2.

The band gap and the optimized crystal structure of $AgInS_2$ in the tetragonal phase were also calculated (Figure S2). The geometry was obtained from the Materials Project library with the lattice parameters $a = b = 5.93$ Å and $c = 11.52$ Å and the angles $\alpha = \beta = \gamma = 90°$. After relaxation, the volume of the cell was reduced by 3.3% and the lattice constants were obtained as $a = b = 5.85$ Å and $c = 11.42$ Å without changing its angles. The band gap of $AgInS_2$ in the tetragonal phase was found to be 0.36 eV. The crystal structure of $AgInS_2$ attained via experimental synthesis exists in an orthorhombic phase, hence the computational conclusions drawn for the orthorhombic phase is discussed hereafter, except otherwise identified.

2.2. Synthesis and Crystal Structure. The synthesis process of $AgInS_2$−TiO_2 is illustrated in Figure 5. Typically, the TiO_2 nanoparticles prepared by the sol−gel method undergo solvothermal process resulting in the in situ formation of the $AgInS_2$ nanoparticles.[47] This results in a uniform distribution of the dopant particles and formation of close intimate heterojunctions as discussed in the latter sections. The challenges of synthesizing these semiconductor nanostructures are their stability, controlling the stoichiometric composition, and the crystal structure.[37,38,56] As similar to other bulk materials, the nanoparticles of the ternary compounds exhibit interesting electronic and optical properties compared to their bulk counterparts.[57] The formation of the low-temperature
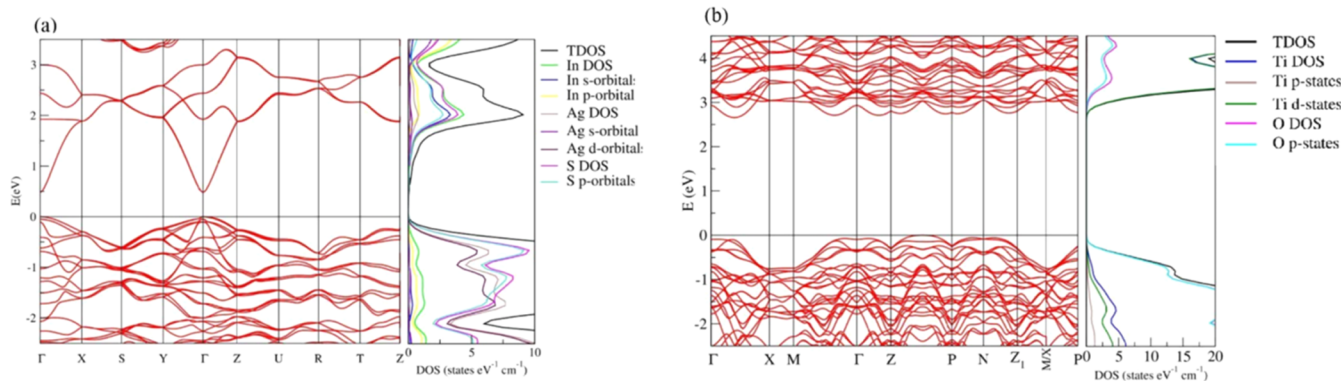

Figure 3. Calculated band structure of (a) $AgInS_2$ and (b) TiO_2 with the corresponding PDOS. The top of the valence band (horizontal line) is aligned at 0 eV.
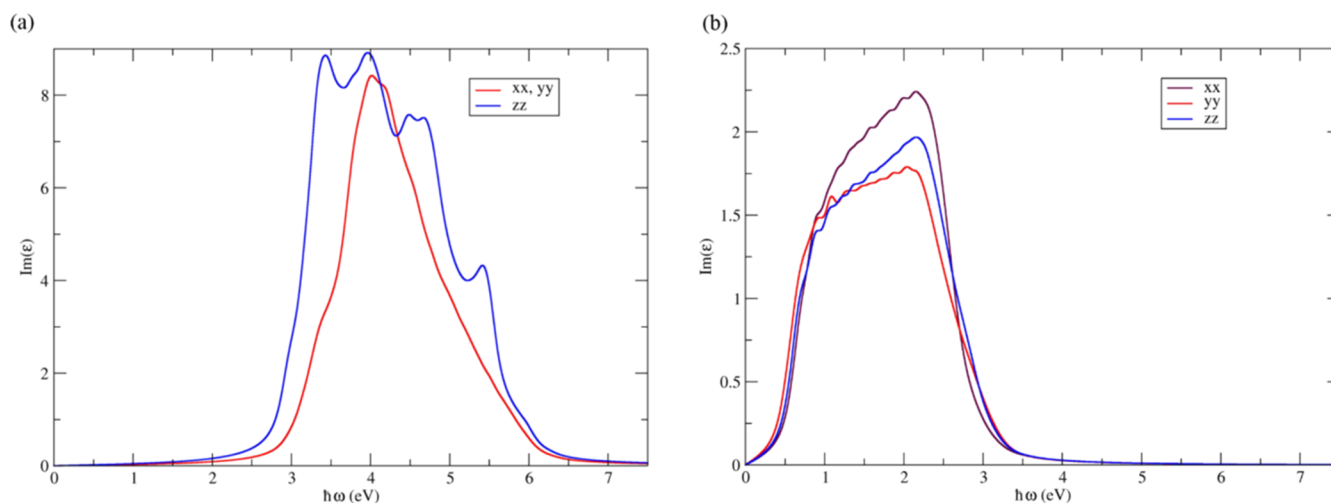
Figure 4. Imaginary part of the dielectric function $(Im(\varepsilon))$ of (a) TiO_2- and (b) $AgInS_2$-calculated infrared, visible, and ultraviolet regions.
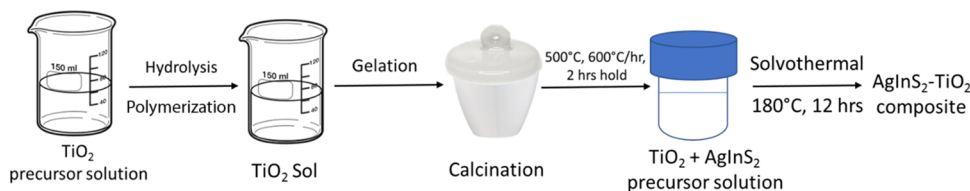

Figure 5. Schematic illustration of the synthesis mechanism of $AgInS_2-TiO_2$ composites.

stable orthorhombic structure of $AgInS_2$ could be ascribed to the solvent picked for the reaction and the balanced use of the two cationic precursors used in the synthesis process. The appropriate reaction temperature and time aid in tuning the reactivity of Ag and In precursors (as observed in the diffractograms of time and temperature studies of $AgInS_2$). As Ag^+ is a soft Lewis acid, therefore appropriate Lewis base such as ethanolamine (EA) is used as a suitable ligand required for the complexation process. Moreover, the presence of lone nitrogen chelating atom on an amine molecule makes EA, a potential structure forming mediator.[58,59]

The formation of $AgInS_2$ nanoparticles using a solvothermal technique could be explained as follows

$$AgNO_3 + EA \rightarrow Ag(EA)_x^+ + NO_3^- \qquad (1)$$

$$In(NO_3)_3 + EA \rightarrow In(EA)_y^{3+} + 3NO_3^- \qquad (2)$$
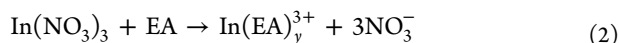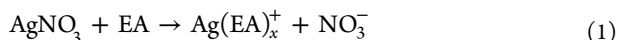
At the beginning of the reaction, the Ag^+ and In^{3+} ions form covalent complexes as given above (where x and y are positive integers), due to the use of EA as a solvent.[60,61] Additionally, these complexes react with thiourea (TH) resulting in the formation of complexes as

$$Ag(EA)_x^+ + xTH \rightarrow [Ag(TH)_x]^+ + EA \qquad (3)$$

$$In(EA)_y^{3+} + yTH \rightarrow [In(TH)_y]^{3+} + EA \qquad (4)$$
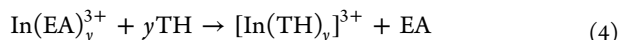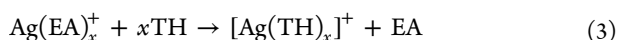
The formation of any free radicals of S^{2-} from thiourea is proposed to be prevented to some extent, due to the use of EA as a solvent. This mechanism averts the creation of any additional binary impurity phases, for example, In_2S_3 or Ag_2S. The stability of thiourea falls on enhancing the temperature and eventually results in the formation of more stable ternary chalcogenide phase to yield $AgInS_2$. Meanwhile, the thiourea in the reaction plays a dual nature partly by aiding in the

formation of a complex and also as a source of sulfur other than thiourea.[62,63]

$$[Ag(TH)_x]^+ + [In(TH)_y]^{3+} \rightarrow AgInS_2 \qquad (5)$$
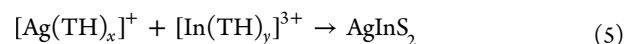
The structure and the crystallinity of the as-synthesized $AgInS_2-TiO_2$ composites were investigated using X-ray diffractogram (XRD). Figure 6 displays the formation of the
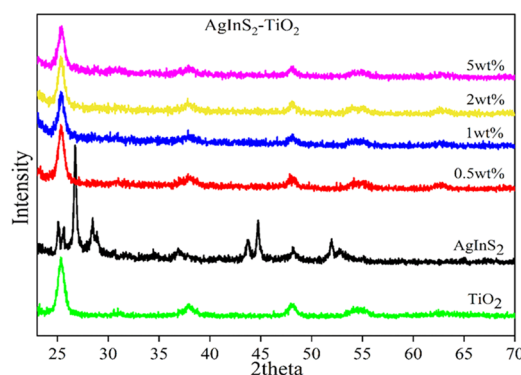

Figure 6. X-ray diffractograms of $AgInS_2$, TiO_2, and $AgInS_2-TiO_2$ composites.

as-prepared $AgInS_2$ and $AgInS_2-TiO_2$ composites. Orthorhombic phase of $AgInS_2$ [$a = 7.00$ Å, $b = 8.28$ Å, $c = 6.69$ Å, and $\alpha = \beta = \gamma = 90°$] with peaks defining at 24.90, 25.40, 26.80, 28.50, 36.70, 43.67, 44.78, 48.23, and 51.80° owing to (120), (200), (002), (121), (122), (040), (320), (203), and (042), respectively, is observed [JCPDS -00-025-1328].[46] The XRD peak intensity at 26.8° of the (002) plane shows a higher intensity. Although, the primary peak in the given case might reflect the formation of the tetragonal phase. However, the presence of prominent peaks at 24.9, 25.4, and 28.5° prove

otherwise. The tetragonal phase of $AgInS_2$ does not exhibit any peaks at <26° (2Θ value). The slightly widened peaks could be attributed to the decreased nanocrystal size as observed in the transmission electron microscopy (TEM) images (Figure 15) and also observed in the previous reports.[64−66] Moreover, the Raman results aid in confirming the orthorhombic phase as the peaks at 264 and 316 cm^{-1} correspond to the orthorhombic wurtzite structure, while the peaks of the tetragonal phase only appear at 240 and 345 cm^{-1}, which are absent in this case (the inset of Figure 12).[43,46,67,68]

The diffractograms in Figure 7 compare the as-synthesized $AgInS_2$ with other peaks of Ag_2S [JCPDS 00-014-0072], In_2S_3
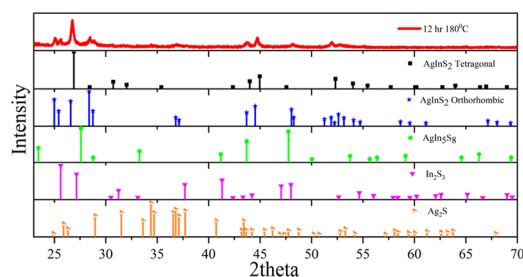

Figure 7. XRD of as-prepared $AgInS_2$ with other standard peaks of $AgInS_2$ orthorhombic, $AgInS_2$ tetragonal, Ag_2S, and In_2S_3.

[JCPDS 00-033-0624], $AgIn_5S_8$ [JCPDS 00-026-1477], and $AgInS_2$ tetragonal [JCPDS 00-025-1330]. It displays the orthorhombic $AgInS_2$ formation, deprived of any impurity.

The temperature and time studies were accomplished, with the purpose of optimizing the reaction parameters for solvothermal synthesis. Figure 8a illustrates the temperature study of $AgInS_2$ at altered temperatures (150−250 °C) for 12 h. The crystallinity of the sample increases with the rise in temperature from 150 to 180 °C (the peak observed at 26.80°). The intensity of the identical peak declines on increasing the temperatures after 200−250 °C. Therefore, 180 °C was applied as an ideal temperature for further assessing the time period for this solvothermal synthesis. Figure 8b exhibits the outcome of time study, which demonstrates the surge in the crystallinity of the peak at 26.10° on enhancing the time duration from 6 h to 12 h. The intensity of the peak at 26.80° decreases on assessment up to 72 h of the synthesis period. Therefore, 180 °C for 12 h is reflected as the optimum solvothermal parameters for $AgInS_2$.

Figure 6 also exhibits the diffractograms of TiO_2 and its composites with $AgInS_2$. Peaks corresponding to $AgInS_2$ are no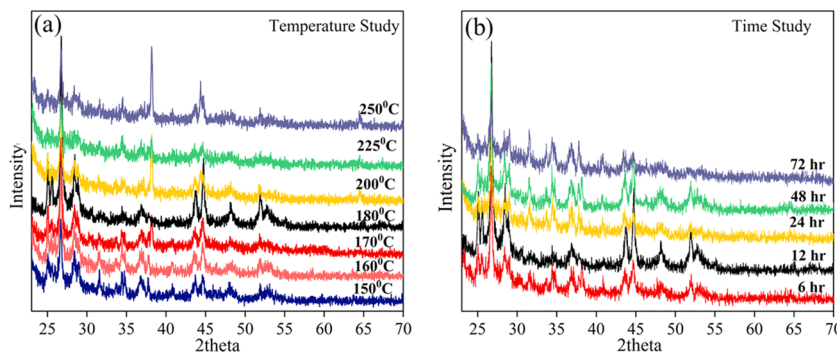t observed in the current diffractogram, which is endorsed to the high crystallinity of the TiO_2 nanoparticles and the small doping amount of $AgInS_2$. Sharp peaks of TiO_2 [$a = b = 3.78$ Å and $c = 9.50$ Å] at 25.40, 38.50, 48.00, and 55.00° to (101), (112), (200), and (211) correspondingly are likewise displayed in the diffractogram.[69,70]

The composite structures as exhibited in Figure 6 neither showed any change in crystallinity nor there is any indication of rutilation (impurity phase) of TiO_2. Moreover, the lattice constant acquired for the bare samples presented a decent agreement to the computationally obtained values. The 0.5 wt % $AgInS_2–TiO_2$ composites demonstrated the top photocatalytic outcomes (as shown in the latter segments) amid their parent and other dopant % samples. Therefore, henceforward, it is used for additional characterizations except otherwise identified.

2.3. Optical Properties. To examine the optical absorption behavior of the as-synthesized materials, UV−vis diffuse reflectance spectroscopy (DRS) spectra were employed. Figure 9 shows the diffused reflectance spectra of titania and
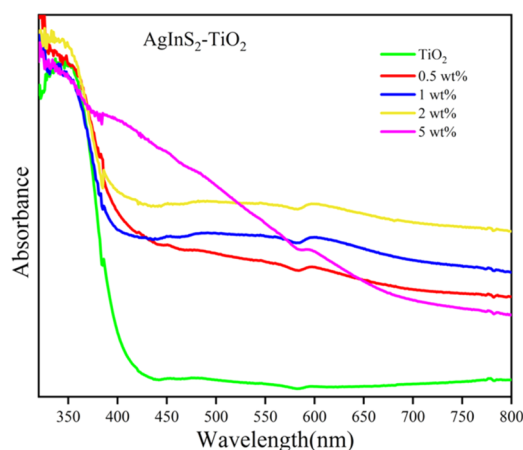

Figure 9. DRS spectra of TiO_2 and $AgInS_2–TiO_2$ composites.

$AgInS_2–TiO_2$ composites. TiO_2 exhibits a maximum at 350 nm (UV region), which corroborates the computationally obtained first peak of the imaginary part of the dielectric spectra at 3.8 eV. A substantial improvement in the absorption in the visible region is detected in $AgInS_2–TiO_2$ materials.[70] The composite samples exhibited the signature sharp hump of TiO_2 at 380 nm; however, the absorption edge is extended up to 800 nm.

The indirect band gap measurements of the composite samples and titania are assessed, as shown in Figure 10. Thus,
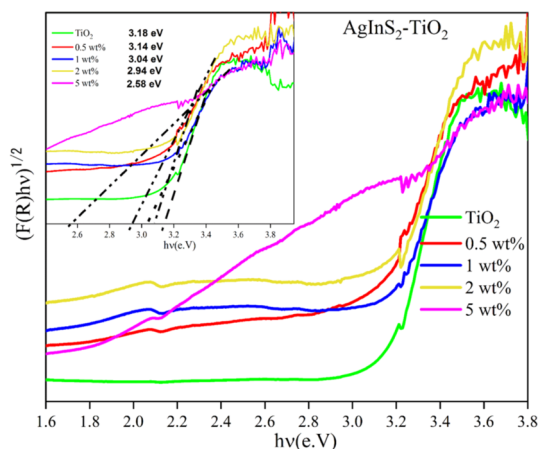

Figure 8. (a) Temperature and (b) time studies of $AgInS_2$ solvothermal synthesis.

Figure 10. Band gap estimation of titania and AgInS$_2$–TiO$_2$ composites.

Figure 12. Raman analyses of AgInS$_2$, TiO$_2$, and AgInS$_2$–TiO$_2$ composites.

this substantiates the results computed theoretically (Figures 3b and 4a). The composite samples show a decreased band gap value with an increase in the AgInS$_2$ content. This effectively proves the successful doping of the sample and the formation of the heterostructure.[47]

Figure 11a illustrates the DRS spectra of AgInS$_2$, it shows an enhanced visible light absorption, and the edge extending up to 800 nm. The corresponding band gap is also calculated and shown in Figure 11b. As observed through the absorption spectra, a high visible light absorption resulted in a small band gap of 1.95 eV, which is consistent with the theoretically computed results as discussed in an earlier section (Figures 3a and 4b). The first peak of the imaginary part of the dielectric spectra obtained at 2.04 eV restates the experimental findings of absorption maxima observed at 600 nm (Figure 4b).

The Raman analyses of titania, AgInS$_2$, and AgInS$_2$–TiO$_2$ are illustrated in Figure 12. Characteristic vibrational peaks of the wurtzite structure of AgInS$_2$ are observed at 264 and 316 cm^{-1} (as shown in the inset).[43,46] Apart from that, characteristic bands for titania are detected at 147, 197, 396, 516, and 638 cm^{-1} for A$_{1g}$, ^{2}B$_{1g}$, and ^{3}E$_g$ correspondingly attributed to the anatase phase.[69,71]

Sharp and symmetric peaks of anatase appear in the case of the composite sample and a red shift is also detected for the composite maxima (as specified in the inset of Figure 12), and this successfully proves the efficient doping of the TC atoms into the TiO$_2$ host material. Moreover, the Raman spectra of the composite do not show the existence of any other impurity
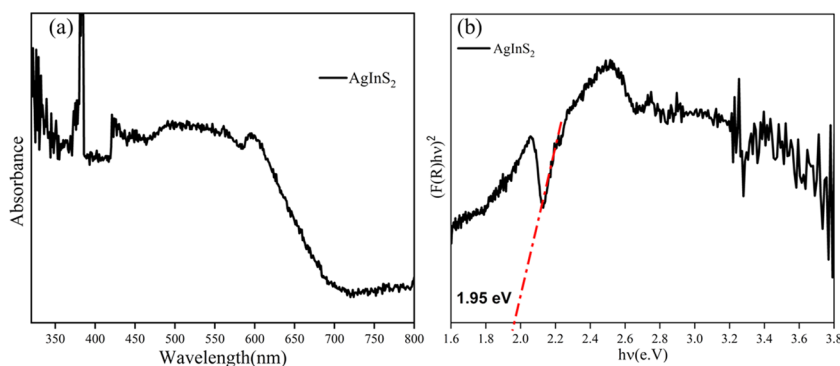
peaks, which corroborates to the inferences observed in XRD.[72,73]

The recombination rate of the solar light-generated electron–hole pair is evaluated using the photoluminescence (PL) measurement. The PL spectra of AgInS$_2$–TiO$_2$ and TiO$_2$ are displayed in Figure 13 (mass normalized). The emission
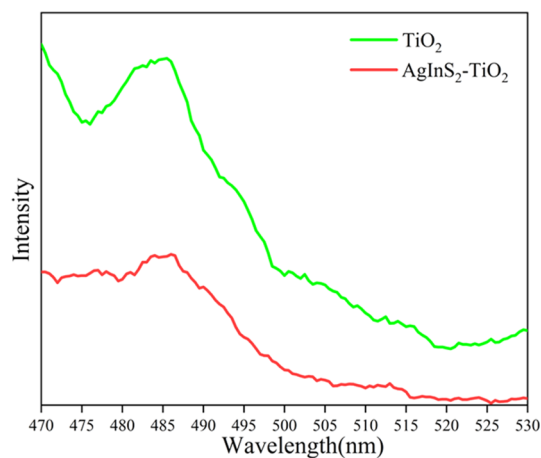
Figure 13. Photoluminescence spectra of AgInS$_2$–TiO$_2$ and TiO$_2$.

peak intensity of AgInS$_2$–TiO$_2$ is reduced compared to TiO$_2$. The lesser PL intensity specifies the poor rate of recombination of electron–hole pairs. This suggests that the introduction of AgInS$_2$ results to retardation in the recombination rate of

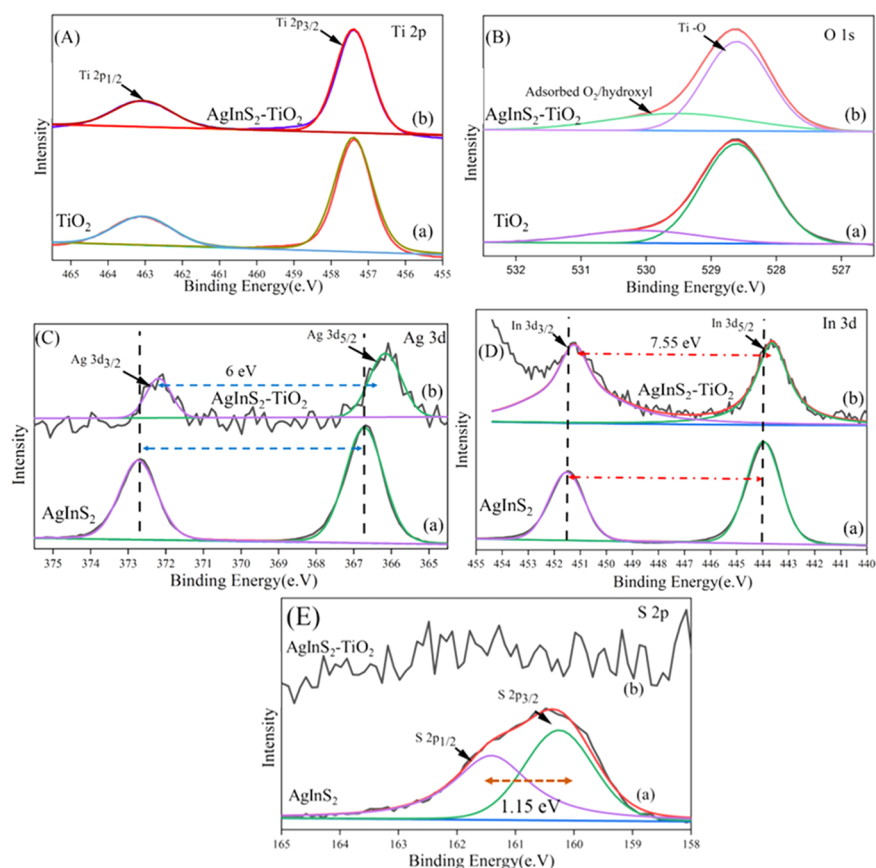**Figure 11.** (a) DRS spectra of AgInS$_2$. (b) Band gap estimation of AgInS$_2$.

Figure 14. High-resolution deconvoluted spectra of (A) Ti 2p (a) titania and (b) AgInS$_2$−TiO$_2$; (B) O 1s (a) TiO$_2$ and (b) AgInS$_2$−TiO$_2$; (C) Ag 3d (a) AgInS$_2$ and (b) AgInS$_2$−TiO$_2$; (D) In 3d (a) AgInS$_2$ and (b) AgInS$_2$−TiO$_2$; and (E) S 2p (a) AgInS$_2$ and (b) AgInS$_2$−TiO$_2$.
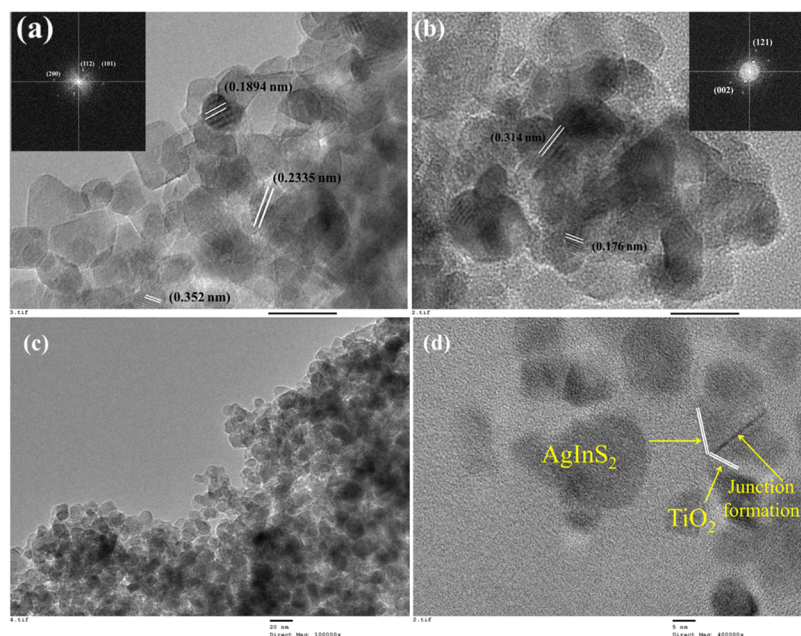
Figure 15. TEM pictures of (a) Titania; (b) AgInS$_2$; and (c), (d) AgInS$_2$−TiO$_2$.

the excitons, which overwhelmingly improves the photocatalytic efficiency.

2.4. Chemical Composition Analysis. The chemical environment and the bonding characteristics are analyzed using X-ray photoelectron spectroscopy (XPS). The survey spectra exhibit the presence of Ti 2p and O 1s in spectra of TiO$_2$. Peaks of Ti 2p, O 1s, Ag 2d, In 3d, and S 2p were observed for AgInS$_2$−TiO$_2$ composites. Very low intensity peaks of C 1s and N 1s are also detected among all of the materials, which might be acquired through the experimental or analysis procedure. Figure 14A illustrates the Ti 2p spectra of titania (a) and the composite of AgInS$_2$−TiO$_2$ (b).

Figure 16. (a) and (b) HRTEM images of AgInS$_2$−TiO$_2$.

Peaks of Ti 2p$_{3/2}$ are observed at 457.8 eV, assigned to Ti^{+4}. The Ti 2p peaks remained unaltered in both cases. Moreover, the O 1s spectra illustrated in Figure 14B show no change in the values of 528.59 and 530.40 eV consistent to crystal lattice oxygen of (O−Ti^{4+}) and adsorbed O$_2$ molec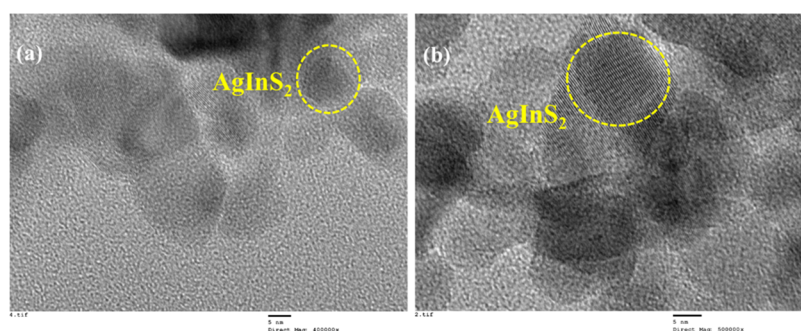ules correspondingly in TiO$_2$ (a) and AgInS$_2$−TiO$_2$ (b) samples.[33,74,75] The Ag 3d high-resolution spectra for both AgInS$_2$ (a) and AgInS$_2$−TiO$_2$ structure (b) are displayed in Figure 14C.

The signature points of Ag 3d$_{3/2}$ and Ag 3d$_{5/2}$ are detected at 372.73 and 366.72 eV correspondingly for the AgInS$_2$ sample.[76,77] The peak shifts slightly to 372.1 and 366.1 eV for the AgInS$_2$−TiO$_2$ sample.[44] Nevertheless, the doublet separation of the Ag 3d oxidation state remained unaltered (6 eV).[78] A similar shift in peaks is observed for In 3d peaks at 451.52 and 443.97 eV corresponding to In 3d$_{3/2}$ and In 3d$_{5/2}$, respectively, to 451.24 and 443.63 eV for AgInS$_2$−TiO$_2$ (Figure 14D). The doublet separation of 7.55 eV was observed for the In 3d peaks, consistent with the previous literature.[79] Figure 14E illustrates the high-resolution spectra of S 2p. Peaks at 161.41 and 160.26 eV correspond to the S 2p$_{1/2}$ and S 2p$_{3/2}$ are observed for AgInS$_2$ samples (doublet splitting of 1.15 eV).[80] Apparently, significant peaks of sulfur were not detectable in that same region; however, broad peak around 161.4 eV is noticed. The peak location of all of the elements is summarized in Table S2.

Thus, the effective interaction amid the heterostructure elements results in the rise in electron concentration, which leads to the interfacial charge transfer causing the shift of the peak detected. The effective electron screening results in the increase in electron concentration leading to a decrease in binding energy.[81−84]

2.5. Morphological and Microstructure Analysis. The transmission electron microscopy (TEM) is employed to evaluate the morphology and microstructure of the samples prepared. The TEM of titania and its selected area diffraction pattern is demonstrated in Figure 15a. The nanoparticles exhibited ovular features, and the typical size was observed to be around 25−40 nm. The interplanar spacing (d) values obtained for diverse areas of the image confirm the formation of the anatase phase of the nanoparticles.[85] Figure 15b illustrates the TEM image of pristine orthorhombic AgInS$_2$. The nanoparticles likewise displayed ovular nature, and the clear lattice fringes were identified of (002) and (121) planes with respective interplanar spacing values of 0.314 and 0.176 nm are observed.

In the meantime, Figure 15c,d shows the TEM images of AgInS$_2$−TiO$_2$ composites. The presence of asymmetric particles identified as AgInS$_2$ in TiO$_2$ is observed. However, the existence of the nanoparticles demonstrates that both

AgInS$_2$ result in intimate integration with the TiO$_2$ nanoparticles, and thus result in the formation of the heterostructure.[47,86] High-resolution TEM (HRTEM) images of the composites are further provided in Figure 16.

2.6. Photocatalytic Applications. *2.6.1. Photodegradation.* Pharmaceutical effluent has grown to be a major contaminant source in rivers and groundwater. The rise in contamination shall result in the growth of antibiotic-resistant bacteria in the water bodies. Hence, effective secondary wastewater treatment has resulted to be an imperative solution to this crisis. Photocatalysis is an excellent alternative, and hence in this study, doxycycline (DC) is used as a modal antibiotic to assess the photocatalytic efficiency of AgInS$_2$−TiO$_2$. The photocatalytic trials were done under dark and solar light illumination correspondingly.[87] Figure 17 demonstrates
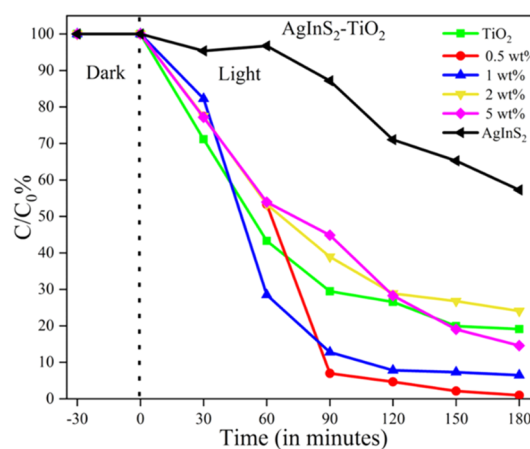
Figure 17. Concentration change of DC with time with TiO$_2$, AgInS$_2$, and AgInS$_2$−TiO$_2$ composites.

the degradation pattern of AgInS$_2$−TiO$_2$ materials by presenting the variation in DC amount (in concentration) with time [C/C_0 % vs time]. As illustrated in Figure 18, the pristine parent and the composite sample displayed no adsorption activity. Moreover, the DC solution (blank sample) exposed under the same condition did not report any change in the profile and thus nullified any possibility of photodecomposition.

Under visible light irradiation, the AgInS$_2$−TiO$_2$ composites exhibit remarkable photocatalytic efficacy as compared to the TiO$_2$ and AgInS$_2$ exposed under the same condition. The pristine TiO$_2$ and AgInS$_2$ presented the least activity compared to the composite samples. The AgInS$_2$, even though having a lower band gap value, is not sufficient to display enhanced

413

Figure 18. (a) Cyclic study and (b) results of species trapping experiment of 0.5 wt % $AgInS_2-TiO_2$.

results. This might be ascribed to the higher recombination of the photogenerated excitons (e−h pairs). Although all of the composites unveiled remarkable degradation profiles, the 0.5 wt % material showed the best and the 5 wt % of $AgInS_2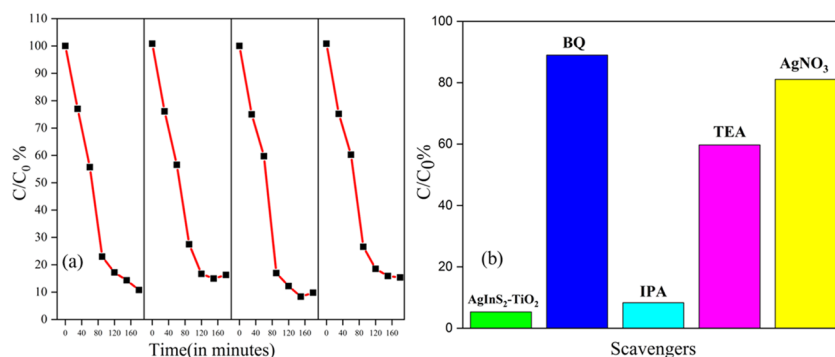-TiO_2$ composite presented the lowest activity within 180 min of irradiation. Henceforth, it could be said that the composites display the best outcomes simply at lesser addant ratios. These effects might be additionally confirmed by the hydrogen generation outcomes as conferred in the later section.

So, as to assess the reusability competence of the materials, the used sample was washed, dried, and reused after every single photocatalytic study. The C/C_0 % vs time graph of 0.5 wt % $AgInS_2-TiO_2$ is illustrated in Figure 18a. The degradation profile remained unaltered even after 4 cyclic runs, and this illustrates the efficiency and the stability of the catalyst prepared. The scavenging experiment was also completed to clarify the contribution of the potential reactive oxygen species associated with the degradation phenomenon. Scavenger chemicals, $AgNO_3$, triethanolamine, benzoquinone (BQ), and isopropyl alcohol (IPA), were added to the degradation system. As observed in Figure 18b, it compares the degradation profiles of 0.5 wt % $AgInS_2-TiO_2$ with the 4 sets of systems in the reaction mixture on irradiated, under the same irradiation condition. The decrease in the activity was considerably altered on the introduction of silver nitrate and BQ. Thus, electrons and holes are observed to be the major active entities in the reaction mixture. Moreover, the IPA-added reaction mixture also exhibited a nominal decrease, which outwardly demonstrates that hydroxyl radicals are not the key players in the photocatalytic activity. Therefore, electron and holes might be established as the key reactive oxygen elements for $AgInS_2-TiO_2$. Moreover, Liu et al. and Zhang et al. studied $AgInS_2-TiO_2$ for various applications. They verified the results of the scavenging experiments by the electron paramagnetic resonance (EPR) technique. The composite samples did not display any signal under dark, while on light irradiation, the $AgInS_2-TiO_2$ displayed four peak intensities for DMPO-O_2*. The DMPO-OH⁻ exhibits a very weak signal intensity, hence substantiating to the results observed in the scavenging experiments.[47,88] Nevertheless, earlier results of EPR on TiO_2 and $AgInS_2$ parent samples indicate the formation of superoxide radicals. He et al. studied the major reactive species generated on visible light irradiation on $AgInS_2$ nanoparticles.[89] Weak signals of hydroxyl and singlet oxygen were observed; however, superoxide radicals exhibited strong signals, which concluded it as the major species in the study. Similarly, anatase TiO_2 illustrates weak signals for hydroxyl and singlet oxygen for UV light irradiation,

and strong peaks were observed for superoxide radicals. The visible light illumination also left weak signals for all of the three major species.[90,91]

The gas chromatography−mass spectrometry and high-performance liquid chromatography−mass spectrometry are utilized to identify the polar and nonpolar intermediates generated in the photocatalytic degradation process.[92] The chromatograms observed aid to define the possible degradation pathway of the pollutant. Zhu et al. define a plausible degradation pathway, as illustrated in Figure 19.[92] The holes
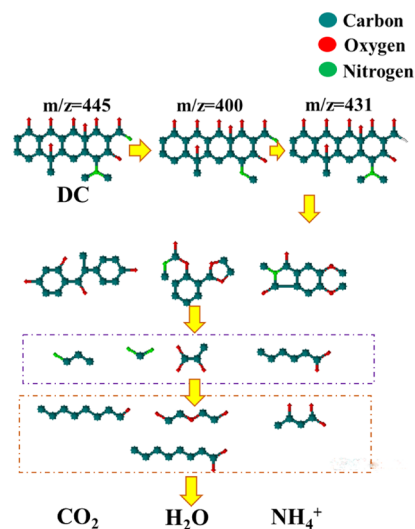
Figure 19. Graphic image of a possible photocatalytic degradation trail of doxycycline.

generated in the process accept electrons from the pollutant molecules and result in the formation of intermediate products. In the very initiation of the process, DC molecules change from a m/z ratio of 445 to m/z of 431 by losing an N-methyl group and resulting in formation of anionic species. Additional degradation leads to generation of intermediates at m/z 400. A continuous light exposure results in further mineralization resulting in the complete disintegration of the DC molecule. The resulting disintegrated smaller parts of the complex structure undergo additional oxidation and lead to generation of smaller organic molecules such as acids and alcohols.[92−94]

2.6.2. Photocatalytic H_2 Production. With the aim of evaluating the photocatalytic competence, the synthesized composites of $AgInS_2$ were investigated for H_2 generation. Visible light-induced water splitting and photoreforming of organic species in aqueous solution have been considered as

414

Figure 20. (a) Rate of hydrogen generation and (b) influence of the pH of the solution at different doping percentage of $AgInS_2-TiO_2$. $[CH_3OH]$ = 10 vol %; sample added = 500 mg/L at RTP.
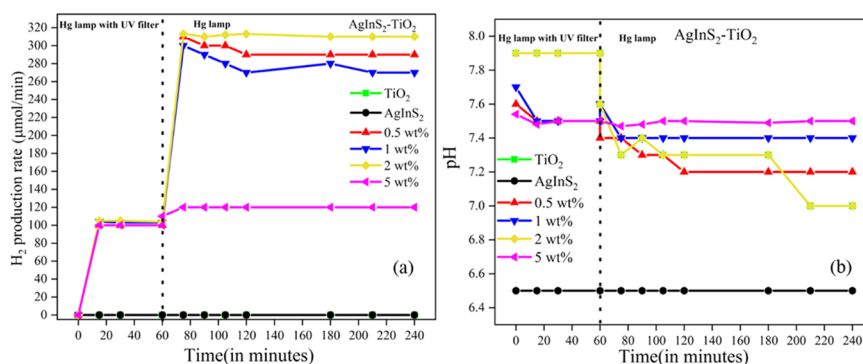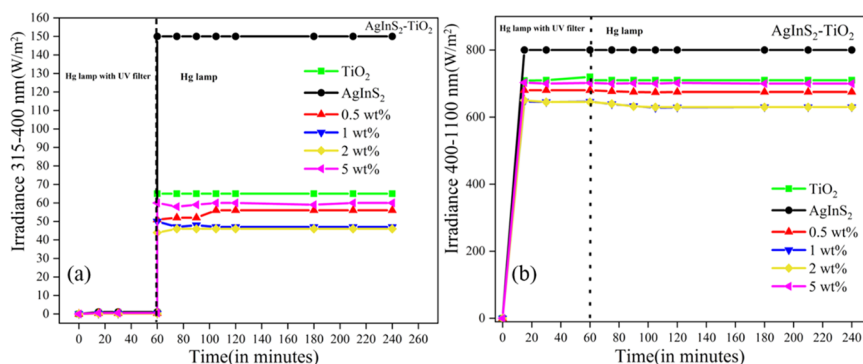

Figure 21. Illumination recorded at the exterior of the reactor walls amid (a) 315−400 nm and (b) 400−1100 nm at different doping ratios of $AgInS_2-TiO_2$ samples. $[CH_3OH]$ = 10 vol %; sample added = 500 mg/L at RTP.

crucial processes to convert solar to chemical energy. The use of sacrificial organic agents helps to obtain higher photo-efficiency due to the oxidation of organic species by photogenerated positive holes, with the simultaneous production of H^+ ions. Photogenerated electrons on the surface of the catalyst encounter with hydrogen ions to produce hydrogen gas. Therefore, merging organic wastewater supervision and H_2 generation via sunlight might be an encouraging sustainable approach to tackle environmental and energy issues.

The H_2 generation rate of $AgInS_2-TiO_2$-synthesized materials together with their bare samples ($AgInS_2$ and TiO_2) was measured. Methanol ($[CH_3OH]$ = 10 vol %) as a sacrificial agent was utilized in this experimental process. As shown in Figure 20a, the catalysts tested show appreciable hydrogen production for 0.5, 1, and 2 wt % for all over the photocatalytic runs. The composite at low dopant % exhibited H_2 output as high as 310 μmol/min. On the contrary, the parent pristine samples ($AgInS_2$ and TiO_2) showed 0 μmol/min. The composite structure exhibits efficient output at lower wt % (up to 2); on increasing the dopant value to 5 wt %, the photocatalytic efficiency decreases. With respect to the starting pH values of the solution, no noteworthy variations have been logged for the $AgInS_2-TiO_2$ composite materials during the illumination duration (Figure 20b).

The illumination measures recorded in the ultraviolet and visible regions of the electromagnetic spectrum on the exterior surface of the apparatus for various $AgInS_2-TiO_2$ samples tested are reported in Figure 21a,b, respectively.

Subsequently, eliminating the ultraviolet A filter, a prompt surge to the UV illuminance measure has been logged. The higher illuminance values herein logged for the $AgInS_2$ material

indicating a lesser suspension absorption, thus resulting in the absence of photocatalytic hydrogen generation. The illumination measures obtained from the outer walls of the reactor did not exhibit any prominent alteration at the visible region. On comparing the irradiance values with hydrogen production rates in the visible region for samples with different composition in weight percentage, it can be stated that higher radiation absorption values (i.e., lower irradiance values recorded on the photoreactor walls) result in slightly improved hydrogen generation rates. In accordance with pecking order of irradiance values in the visible region, the photocatalytic activity had the following sequence: 2% $AgInS_2-TiO_2$ > 1% $AgInS_2-TiO_2 \approx$ 0.5% $AgInS_2-TiO_2 \gg$ 5% $AgInS_2-TiO_2$.

2.6.3. Photocatalytic Antimicrobial Studies. The photocatalytic efficacy of $AgInS_2-TiO_2$ samples with their pristine parent samples was also studied by light-induced microbial disinfection using a suspension test. A sample mixture with the bacterial inoculate and catalyst was placed under both dark and light environments, respectively.

Additionally, bare materials (only with microbial strains) were too illuminated devoid of the presence of any sample. On irradiating bacterial cells under visible light by catalysts, these displayed higher photocatalytic proficiency by the $AgInS_2-TiO_2$ samples compared to their parent materials. More than a 5-log decrease was achieved in 30 min of illumination for $AgInS_2-TiO_2$ (Figure 22).

The development of the 2 strains was constant in light and dark environments devoid of the presence of any photocatalysts. The bacterial progression of the $AgInS_2$ parent sample displayed a complete antibacterial efficiency only after 80 min. In the case of pristine TiO_2, the total bacterial
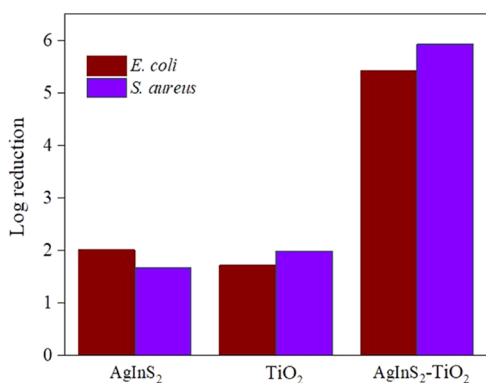
Figure 22. Log reduction of microbial strains with $AgInS_2$, titania, and $AgInS_2-TiO_2$ on 30 min of light irradiation.

inactivation for both the strains was reached only after 60 min of light illumination.

The pictures of agar plates with bacteriological clusters at different periods for $AgInS_2-TiO_2$ are given in Figure 23. All
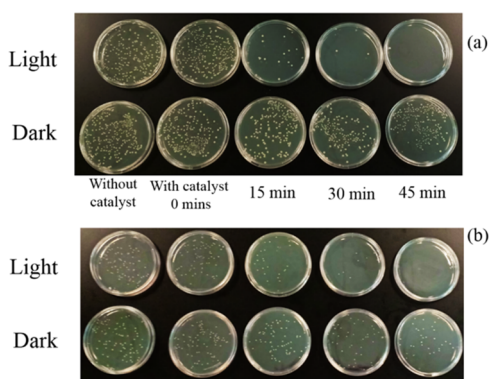

Figure 23. Photographic illustration of reduction of (a) *Escherichia coli* colonies and (b) *Staphylococcus aureus* colonies on agar plates at different periods using $AgInS_2-TiO_2$.

of the composite samples were more active than their parent samples. This could be attributed to the enhanced photocatalytic efficiency of the composite sample. None of the test samples showed any bacterial disinfection property under dark conditions.

2.7. Photocatalytic Mechanism. The composite design of $AgInS_2$ using TiO_2 displayed remarkable photocatalytic performance when equated to their bare materials. The computational results of the electronic and optical properties of $AgInS_2$ and TiO_2 helped in corroborating with the experimentally obtained orthorhombic and tetragonal phases, respectively. Additionally, the band structure and PDOS investigation illustrate that the Ti 3d orbital of TiO_2 dominates the valence band, while the 2p orbital of oxygen is dominated by the conduction band. Similarly, the In−S interaction dominates the conduction band minima of $AgInS_2$, while the Ag−S interaction determines the valence band maxima. Hence, on solar light illumination on the composite structure, the electrons migrate from the 4d orbital of Ag and 3p orbitals of sulfur toward the 5s orbital of In of $AgInS_2$ and latter proceed to the 2p orbital of oxygen in titania.[47,95]

In accordance with the theoretical study, trapping experiments, and the band gap values from UV-DRS, a likely photocatalytic and interfacial electron-transfer mechanism for

$AgInS_2-TiO_2$ heterojunction is illustrated in Figure 24. The conduction band (CB) and valence band (VB) potentials of
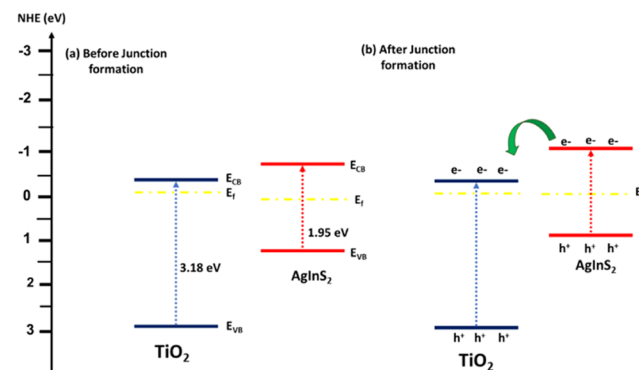

Figure 24. Graphical illustration of the photocatalytic mechanism for $AgInS_2-TiO_2$ (a) before and (b) after heterojunction formation.

the heterostructure components ($AgInS_2$ and TiO_2) are vital to comprehend the migration of photoexcited charge carriers above the nanocomposites. The relevant calculations and the summarized explanation of the process are given in the Supporting Information.

Therefore, by means of the calculated values, as given in the Supporting Information, a likely photocatalytic mechanism is proposed below. The CB and VB edge values of $AgInS_2$ and titania, prior and later the $AgInS_2-TiO_2$ heterojunction creation, are illustrated in Figure 24. Figure 24a displays the Fermi level positions of $AgInS_2$ and titania at 0.27 and −0.1 eV correspondingly. The formation of the heterostructure results in the Fermi levels of $AgInS_2$ and titania to an extent at a uniform level (Figure 24b). Since the dopant level of $AgInS_2$ is extremely low, thus the band position of $AgInS_2$ is altered, and hence the Fermi level of $AgInS_2$ reaches −0.1 eV.[47] The refreshed band edge locations for $AgInS_2$ are found to be at +0.825 and −0.625 eV, as both the VB and CB shift, as shown in Figure 24b. Charged excitons are produced on the surface of titania and $AgInS_2$ on being irradiated with solar light. The holes on the VB of TiO_2 and the holes on the VB of $AgInS_2$ participate in the reaction process individually,[96] while the electrons from the CB of $AgInS_2$ migrate to the conduction band of titania. The electrons participate along with the adsorbed O_2 in the surface of the photocatalyst to form an O_2^* (superoxide) radical. As observed in the result of trapping experiments, the electrons, superoxide radicals, and the holes played the role of predominant species. These radicals were further engaged in photocatalytic reactions.

3. CONCLUSIONS

In summary, the current study reported the fabrication of ternary metal chalcogenide heterostructure nanocomposites of titania. The composite material showcased a dramatic improvement in visible light absorption. The increase in the dopant percent in the composite ensued in the narrowing of the band gap. Furthermore, the shift in the peak signals of XPS suggested an alteration in the chemical surroundings of the heterostructure. Importantly, the degradation outcomes illustrated the enhanced efficiency, and comparable results were observed in the case of the light-induced hydrogen generation. The composite structures displayed 300 times enhanced hydrogen production output when matched with their bare sample materials. A log-5 microbial inactivation was

accomplished in 30 min of light irradiance. A possible interfacial electron transfer and the photocatalytic mechanism are offered based on the computational analysis, species trapping experiment, and also the band gap value estimation from the absorbance plot. Therefore, the current investigation details the positive composite preparation and highlights the multifunctional photocatalytic applications.

4. MATERIALS AND METHOD

4.1. Photocatalyst Preparation. Pristine anatase titania was synthesized by the sol−gel method, using titanium isopropoxide (TTIP) as the precursor. In this experiment, 20 mL of TTIP was suspended in 100 mL of isopropanol. Further on continuous stirring, distilled water was added slowly to the solution of TTIP in isopropanol. The volume of water and isopropanol was equal, and the resultant sol was left for gel formation for 120 min at room temperature. The white colloid gel that formed was allowed to dry for 12 h at 100 °C in an oven. The dried xerogel was ground and further calcined using a muffle furnace at 500 °C, with a gradient rate of 600 °C per h for 2 h.

The one-pot solvothermal method was used to prepare $AgInS_2$−TiO_2 heterostructure composites. A certain quantity of $AgNO_3$, $In(NO_3)_3 \cdot xH_2O$, and thiourea (1:1:2) was vigorously stirred in 30 mL of ethanolamine for 30 min. The prepared TiO_2 was added to the mixture and was sonicated for the next half an hour. The above mixture was transferred into a 50 mL steel Teflon-lined vessel and heated up to 180 °C for 12 h. After being cooled to room temperature, the resultant solid product was washed with water and ethanol multiple times to remove the residue. The washed powder was dried at 60 °C for 12 h and denoted as $AgInS_2$−TiO_2, and it was used for further characterization and applications. The parent sample, $AgInS_2$, was synthesized using the same method without the addition of TiO_2.[47]

4.2. Photocatalytic Activity. To evaluate the photocatalytic efficiency of synthesized $AgInS_2$−TiO_2 samples, photocatalytic degradation of doxycycline (DC) under solar light radiance by means of a photoreactor unit was done. In this experiment, 0.10 g of the photocatalyst was added into 100 mL of DC (10^{-5} M) solution (1 g/L) in water and was stirred for 1 h in dark prior to irradiation to attain absorption−desorption equilibrium. During the illumination period, aliquots were withdrawn at an interval of 15 min. A UV−vis spectrophotometer was used to measure the degradation profiles of the doxycycline with respect to time of the sample aliquots. The reduction in the peak intensity (357 nm) of doxycycline was analyzed. Similarly, the degradation profiles of bare samples (TiO_2 and $AgInS_2$) were performed for a comparative evaluation. To assess the recyclability of the samples, the photocatalysts were subjected to centrifugation, washing, drying, and these were reused after each experiment.

4.2.1. Species Trapping Experiment. Different scavenger tests were performed to analyze the ROS (reactive oxygen species) formed during the catalytic reaction in the mixture. Radical scavengers like isopropanol (10 mM), $AgNO_3$ (6 mM), benzoquinone (6 mM), and triethanolamine (10 mM) were added into separate photocatalytic systems to quench the formed hydroxyl radicals (OH^-), electron, superoxide radicals ($O_2^\bullet$), and holes, respectively. The concentration of catalysts was kept as same as for degradation studies (0.08 g in 80 mL of aqueous DC). These solutions were kept in dark condition for 60 min, and further, they were allowed to expose to light

irradiation for another 180 min. Aliquots were taken at an interval of 15 min and tested for DC concentration for the photocatalytic experiments as explained above.

4.3. Photocatalytic Hydrogen Generation. The photocatalytic hydrogen generation experiments were performed in a 300 mL annular glass batch reactor, which was concealed with an aluminum foil (Figure 25).
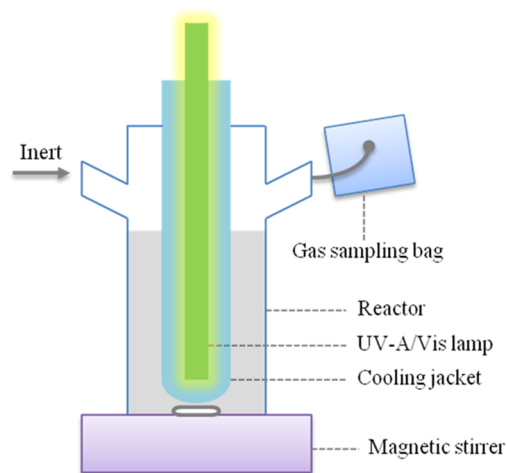

Figure 25. Schematic diagram of the photocatalytic reactor.

A 125 W high-pressure mercury vapor lamp from Helios Italquartz was used as the light source. During the experiments, the temperature of the reactor was maintained at 25 °C using a thermostatic bath (Falc GTR 90). The reactants and gaseous nitrogen were fed into the reactor through an inlet, and gaseous sample aliquots at different times were taken through an outlet.

In a typical H_2 experiment, a fixed amount of the photocatalytic material and CH_3OH solution was added into 300 mL of aqueous solution, and the subsequent solution was fed into the reactor under magnetic stirring. To prevent the unwanted reactions of dissolved oxygen with photogenerated electrons, the solution was flushed with nitrogen gas for 30 min before the photocatalytic runs. Furthermore, nitrogen was continuously fed to the reactor with a flow rate (Q_{N_2}) of 0.3 L/min throughout the experiments.

The pH of the solution was observed with an Orion 420Ap pH-meter (Thermo) during the experiments. The collected liquid aliquots at different time intervals were quickly filtered using regenerated cellulose filters (pore diameter 0.20 μm, Scharlau), and the pH was measured using the filtrate.

The Tedlar gas sampling bags were used to collect the gaseous samples recovered from the outlet, and then the hydrogen concentration is evaluated. A gas chromatograph (Agilent 7820A) equipped with an HP−PLOT Molesieve 5A column (Agilent) and a TCD detector with argon as the carrier gas were used to measure the concentration of hydrogen in the samples.

The radiation that emerged from the reactor was evaluated on the exterior walls of the reactor with radiometers in the wavelength ranges from 315 to 400 and to 400 to 1100 nm during the experiments. 1 M sodium nitrite solution was introduced inside the cooling jacket for maintaining 25 °C temperature during the experiment and to cut-off UVA

radiation emitted from the lamp ($| < 400$ nm) for a fixed reaction time of 60 min in all of the same experiments.

4.4. Photocatalytic Antimicrobial Activity. Bacterial disinfection efficiency of $AgInS_2-TiO_2$ composites was calculated with Gram-negative (*E. coli*) and Gram-positive (*S. aureus*) strains and compared the activity with the parent samples TiO_2 and $AgInS_2$. A fixed concentration of 1 g/L of the catalyst in bacterial suspensions (strain in 0.9% NaCl solution) was taken in a cylindrical glass and placed inside a photochamber under visible light irradiation for 3 h. The concentration of bacterial colonies in the buffer solution was maintained as 10^4 CFU/mL (colony forming units/mL) for all experiments. Aliquots of 1 mL of the cell suspension were taken at fixed time intervals of 15 min. To attain a countable CFU, aliquots were diluted in PBS (phosphate-buffered saline) solution (pH 7), and then 0.1 mL of aliquots was spread onto an agar plate and incubated for 24 h at 37 °C. The viable cells were counted and recorded as CFU/mL. Control experiments were performed with the bare bacterial solution, and all samples were also examined under dark environments. All analyses were conducted in triplicate. Log reduction and $N/N_{0\%}$ vs time plot were utilized to calculate the antimicrobial efficiency.

ASSOCIATED CONTENT

⑤ Supporting Information

The Supporting Information is available free of charge at https://pubs.acs.org/doi/10.1021/acsomega.9b02907.

Chemicals and reagents, characterizations, computational details, photocatalytic degradation calculation, antimicrobial disinfection estimation band gap valuation of titania, $AgInS_2$ and $AgInS_2-TiO_2$ samples; XRD pattern of theoretically optimized orthorhombic $AgInS_2$; optimized crystal structure of tetragonal $AgInS_2$ and its corresponding band structure, equation to calculate the percentage error, tables summarizing the band gap measures of titania, $AgInS_2$ and $AgInS_2-TiO_2$ samples; survey spectra of TiO_2 and $AgInS_2-TiO_2$, tables summarizing the peak positions of $AgInS_2$ and $AgInS_2-TiO_2$, photocatalytic inactivation and band edge position calculation; tables summarizing Ionization energy and the electron affinity values, a table summing the electronegativity value and a table summing the conduction band and valence band values (PDF)

AUTHOR INFORMATION

Corresponding Author

*E-mail: pillai.suresh@itsligo.ie.

ORCID ⑩

Priyanka Ganguly: 0000-0002-2709-2553

Syam Kumar R: 0000-0002-4065-2666

Suresh C. Pillai: 0000-0002-8901-9116

Notes

The authors declare no competing financial interest.

ACKNOWLEDGMENTS

REFERENCES

(1) Lewis, N. S.; Nocera, D. G. Powering the planet: Chemical challenges in solar energy utilization. *Proc. Natl. Acad. Sci. U.S.A.* **2006**, *103*, 15729−15735.

(2) Winter, C.-J. Into the hydrogen energy economy—milestones. *Int. J. Hydrogen Energy* **2005**, *30*, 681−685.

(3) Artz, J.; Müller, T. E.; Thenert, K.; Kleinekorte, J.; Meys, R.; Sternberg, A.; Bardow, A.; Leitner, W. Sustainable conversion of carbon dioxide: an integrated review of catalysis and life cycle assessment. *Chem. Rev.* **2017**, *118*, 434−504.

(4) Ran, J.; Jaroniec, M.; Qiao, S. Z. Cocatalysts in Semiconductor-based Photocatalytic CO_2 Reduction: Achievements, Challenges, and Opportunities. *Adv. Mater.* **2018**, *30*, No. 1704649.

(5) Huang, J.; Yu, H.; Dai, A.; Wei, Y.; Kang, L. Drylands face potential threat under 2 C global warming target. *Nat. Clim. Change* **2017**, *7*, No. 417.

(6) Lan, S.; Zeng, X.; Rather, R. A.; Lo, I. M. C. Enhanced trimethoxypyrimidine degradation by piezophotocatalysis of $BaTiO_3/Ag_3PO_4$ using mechanical vibration and visible light simultaneously. *Environ. Sci.: Nano* **2019**, *6*, 554−564.

(7) Ganguly, P.; Breen, A.; Pillai, S. C. Toxicity of Nanomaterials: Exposure, Pathways, Assessment, and Recent Advances. *ACS Biomater. Sci. Eng.* **2018**, *4*, 2237−2275.

(8) Suyana, P.; Ganguly, P.; Nair, B. N.; Mohamed, A. P.; Warrier, K.; Hareesh, U. $Co_3O_4-C_3N_4$ p−n nano-heterojunctions for the simultaneous degradation of a mixture of pollutants under solar irradiation. *Environ. Sci.: Nano* **2017**, *4*, 212−221.

(9) Ganguly, P.; Harb, M.; Cao, Z.; Cavallo, L.; Breen, A.; Dervin, S.; Dionysiou, D. D.; Pillai, S. C. 2D Nanomaterials for Photocatalytic Hydrogen Production. *ACS Energy Lett.* **2019**, No. 1687.

(10) Chu, S.; Cui, Y.; Liu, N. The path towards sustainable energy. *Nat. Mater.* **2017**, *16*, No. 16.

(11) Roger, I.; Shipman, M. A.; Symes, M. D. Earth-abundant catalysts for electrochemical and photoelectrochemical water splitting. *Nat. Rev. Chem.* **2017**, *1*, No. 0003.

(12) Dou, B.; Zhang, H.; Cui, G.; Wang, Z.; Jiang, B.; Wang, K.; Chen, H.; Xu, Y. Hydrogen production by sorption-enhanced chemical looping steam reforming of ethanol in an alternating fixed-bed reactor: Sorbent to catalyst ratio dependencies. *Energy Convers. Manage.* **2018**, *155*, 243−252.

(13) Arregi, A.; Amutio, M.; Lopez, G.; Bilbao, J.; Olazar, M. Evaluation of thermochemical routes for hydrogen production from biomass: A review. *Energy Convers. Manage.* **2018**, *165*, 696−719.

(14) Grätzel, M. Recent advances in sensitized mesoscopic solar cells. *Acc. Chem. Res.* **2009**, *42*, 1788−1798.

(15) Ong, W.-J. 2D/2D graphitic carbon nitride (g-C_3N_4) heterojunction nanocomposites for photocatalysis: why does face-to-face interface matter? *Front. Mater.* **2017**, *4*, No. 11.

(16) Burakov, A. E.; Galunin, E. V.; Burakova, I. V.; Kucherova, A. E.; Agarwal, S.; Tkachev, A. G.; Gupta, V. K. Adsorption of heavy metals on conventional and nanostructured materials for wastewater

treatment purposes: A review. *Ecotoxicol. Environ. Saf.* **2018**, *148*, 702−712.

(17) Lima, E. C. Removal of emerging contaminants from the environment by adsorption. *Ecotoxicol. Environ. Saf.* **2018**, *150*, 1−17.

(18) Kamat, P. V. Semiconductor surface chemistry as holy grail in photocatalysis and photovoltaics. *Acc. Chem. Res.* **2017**, *50*, 527−531.

(19) Zhang, J.; Ma, Y.; Du, Y.; Jiang, H.; Zhou, D.; Dong, S. Carbon nanodots/WO_3 nanorods Z-scheme composites: remarkably enhanced photocatalytic performance under broad spectrum. *Appl. Catal., B* **2017**, *209*, 253−264.

(20) Huang, Y.; Liang, Y.; Rao, Y.; Zhu, D.; Cao, J.-j.; Shen, Z.; Ho, W.; Lee, S. C. Environment-friendly carbon quantum dots/$ZnFe_2O_4$ photocatalysts: characterization, biocompatibility, and mechanisms for NO removal. *Environ. Sci. Technol.* **2017**, *51*, 2924−2933.

(21) Huang, W.; Ma, B. C.; Lu, H.; Li, R.; Wang, L.; Landfester, K.; Zhang, K. A. Visible-light-promoted selective oxidation of alcohols using a covalent triazine framework. *ACS Catal.* **2017**, *7*, 5438−5442.

(22) Zeng, X.; Lan, S.; Lo, I. M. Rapid disinfection of *E. coli* by a ternary $BiVO_4/Ag/g\text{-}C_3N_4$ composite under visible light: photocatalytic mechanism and performance investigation in authentic sewage. *Environ. Sci.: Nano* **2019**, *6*, 610−623.

(23) Zhang, W.; Li, G.; Liu, H.; Chen, J.; Ma, S.; An, T. Correction: Micro/nano-bubble assisted synthesis of Au/TiO_2@ CNTs composite photocatalyst for photocatalytic degradation of gaseous styrene and its enhanced catalytic mechanism. *Environ. Sci.: Nano* **2019**, *6*, No. 991.

(24) Liu, X.; Iocozzia, J.; Wang, Y.; Cui, X.; Chen, Y.; Zhao, S.; Li, Z.; Lin, Z. Noble metal−metal oxide nanohybrids with tailored nanostructures for efficient solar energy conversion, photocatalysis and environmental remediation. *Energy Environ. Sci.* **2017**, *10*, 402−434.

(25) Ganguly, P.; Byrne, C.; Breen, A.; Pillai, S. C. Antimicrobial Activity of Photocatalysts: Fundamentals, Mechanisms, Kinetics and Recent Advances. *Appl. Catal., B* **2017**, *225*, 51−75.

(26) Pu, S.; Zhu, R.; Ma, H.; Deng, D.; Pei, X.; Qi, F.; Chu, W. Facile in-situ design strategy to disperse TiO_2 nanoparticles on graphene for the enhanced photocatalytic degradation of rhodamine 6G. *Appl. Catal., B* **2017**, *218*, 208−219.

(27) Chen, C.-B.; Li, C.-X.; Zhang, Y.-J.; Wang, Y.-J.; Lu, J.-Y.; Liu, H.-Q.; Li, W.-W. Cyano-rich mesoporous carbon nitride nanospheres for visible-light-driven photocatalytic degradation of pollutants. *Environ. Sci.: Nano* **2018**, *5*, 2966−2977.

(28) Li, Z.; Sun, L.; Liu, Y.; Zhu, L.; Yu, D.; Wang, Y.; Sun, Y.; Yu, M. SnSe@ SnO_2 core-shell nanocomposite for synchronous photo-thermal-photocatalytic production of clean water. *Environ. Sci.: Nano* **2019**, No. 1507.

(29) Low, J.; Yu, J.; Jaroniec, M.; Wageh, S.; Al-Ghamdi, A. A. Heterojunction photocatalysts. *Adv. Mater.* **2017**, *29*, No. 1601694.

(30) Yang, Y.; Liu, G.; Irvine, J. T.; Cheng, H. M. Enhanced photocatalytic H_2 production in core−shell engineered rutile TiO_2. *Adv. Mater.* **2016**, *28*, 5850−5856.

(31) Liu, F.; Zhang, W.; Tao, L.; Hao, B.; Zhang, J. Simultaneous photocatalytic redox removal of chromium (vi) and arsenic (iii) by hydrothermal carbon-sphere@ nano-Fe_3O_4. *Environ. Sci. Nano* **2019**, *6*, 937−947.

(32) Fujishima, A.; Honda, K. Electrochemical photolysis of water at a semiconductor electrode. *Nature* **1972**, *238*, 37.

(33) Etacheri, V.; Seery, M. K.; Hinder, S. J.; Pillai, S. C. Oxygen rich titania: A dopant free, high temperature stable, and visible-light active anatase photocatalyst. *Adv. Funct. Mater.* **2011**, *21*, 3744−3752.

(34) Fisher, M. B.; Keane, D. A.; Fernandez-Ibanez, P.; Colreavy, J.; Hinder, S. J.; McGuigan, K. G.; Pillai, S. C. Nitrogen and copper doped solar light active TiO_2 photocatalysts for water decontamination. *Appl. Catal., B* **2013**, *130*, 8−13.

(35) Li, T.; Shen, Z.; Shu, Y.; Li, X.; Jiang, C.; Chen, W. Facet-dependent evolution of surface defects in anatase TiO2 by thermal treatment: implications for environmental applications of photocatalysis. *Environ. Sci.: Nano* **2019**, No. 1740.

(36) Santra, P. K.; Kamat, P. V. Tandem-layered quantum dot solar cells: tuning the photovoltaic response with luminescent ternary cadmium chalcogenides. *J. Am. Chem. Soc.* **2013**, *135*, 877−885.

(37) Xie, C.; Lu, X.; Deng, F.; Luo, X.; Gao, J.; Dionysiou, D. D. Unique surface structure of nano-sized $CuInS_2$ anchored on rGO thin film and its superior photocatalytic activity in real wastewater treatment. *Chem. Eng. J.* **2018**, *338*, 591−598.

(38) Xu, F.; Zhang, J.; Zhu, B.; Yu, J.; Xu, J. $CuInS_2$ sensitized TiO_2 hybrid nanofibers for improved photocatalytic CO_2 reduction. *Appl. Catal., B* **2018**, *230*, 194−202.

(39) Baek, M.; Kim, E.-J.; Hong, S. W.; Kim, W.; Yong, K. Environmentally benign synthesis of $CuInS_2/ZnO$ heteronanorods: visible light activated photocatalysis of organic pollutant/bacteria and study of its mechanism. *Photochem. Photobiol. Sci.* **2017**, *16*, 1792−1800.

(40) Do, J. Y.; Chava, R. K.; Kim, S. K.; Nahm, K.; Park, N.-K.; Hong, J.-P.; Lee, S. J.; Kang, M. Fabrication of core@ interface: shell structured $CuS@ CuInS_2$: In_2S_3 particles for highly efficient solar hydrogen production. *Appl. Surf. Sci.* **2018**, *451*, 86−98.

(41) Lin, L.-H.; Wu, C.-C.; Lai, C.-H.; Lee, T.-C. Controlled deposition of silver indium sulfide ternary semiconductor thin films by chemical bath deposition. *Chem. Mater.* **2008**, *20*, 4475−4483.

(42) Mao, B.; Chuang, C.-H.; Wang, J.; Burda, C. Synthesis and photophysical properties of ternary I−III−VI $AgInS_2$ nanocrystals: intrinsic versus surface states. *J. Phys. Chem. C* **2011**, *115*, 8945−8954.

(43) Hong, S. P.; Park, H. K.; Oh, J. H.; Yang, H.; Do, Y. R. Comparisons of the structural and optical properties of o-$AgInS_2$, t-$AgInS_2$, and c-$AgIn_5S_8$ nanocrystals and their solid-solution nanocrystals with ZnS. *J. Mater. Chem.* **2012**, *22*, 18939−18949.

(44) Liu, Z.; Tang, K.; Wang, D.; Wang, L.; Hao, Q. Facile synthesis of $AgInS_2$ hierarchical flowerlike nanoarchitectures composed of ultrathin nanowires. *Nanoscale* **2013**, *5*, 1570−1575.

(45) Han, J.; Liu, Z.; Guo, K.; Ya, J.; Zhao, Y.; Zhang, X.; Hong, T.; Liu, J. High-efficiency $AgInS_2$-modified ZnO nanotube array photoelectrodes for all-solid-state hybrid solar cells. *ACS Appl. Mater. Interfaces* **2014**, *6*, 17119−17125.

(46) Feng, Z.; Dai, P.; Ma, X.; Zhan, J.; Lin, Z. Monodispersed cation-disordered cubic $AgInS_2$ nanocrystals with enhanced fluorescence. *Appl. Phys. Lett.* **2010**, *96*, No. 013104.

(47) Liu, B.; Li, X.; Zhao, Q.; Ke, J.; Tadé, M.; Liu, S. Preparation of $AgInS_2/TiO_2$ composites for enhanced photocatalytic degradation of gaseous o-dichlorobenzene under visible light. *Appl. Catal., B* **2016**, *185*, 1−10.

(48) Cui, X.; Gu, H.; Guan, Y.; Ren, G.; Ma, Z.; Yin, Y.; Liu, J.; Cui, X.; Yao, L.; Yin, Y. Fabrication of AgInS2 nanoparticles sensitized TiO_2 nanotube arrays and their photoelectrochemical properties. *Appl. Catal., B* **2015**, *137*, 101−106.

(49) Yin, J.; Jia, J.; Yi, G. Synthesis and photoelectric application of AgInS2 clusters. *Mater. Lett.* **2013**, *111*, 85−88.

(50) Ganguly, P.; Mathew, S.; Clarizia, L.; R Kumar, S.; Akande, A.; Hinder, S.; Breen, A.; Pillai, C. S. Theoretical and experimental investigation of visible light responsive $AgBiS_2$ -TiO_2 heterojunctions for enhanced photocatalytic applications. *Appl. Catal., B* **2019**, DOI: 10.1016/j.apcatb.2019.04.033.

(51) Perdew, J. P.; Levy, M. Physical content of the exact Kohn-Sham orbital energies: band gaps and derivative discontinuities. *Phys. Rev. Lett.* **1983**, *51*, 1884.

(52) Tran, F.; Blaha, P.; Schwarz, K. Band gap calculations with Becke−Johnson exchange potential. *J. Phys.: Condens. Matter* **2007**, *19*, No. 196208.

(53) Crowley, J. M.; Tahir-Kheli, J.; Goddard, W. A., III. Resolution of the band gap prediction problem for materials design. *J. Phys. Chem. Lett.* **2016**, *7*, 1198−1203.

(54) Liu, J.; Chen, S.; Liu, Q.; Zhu, Y.; Lu, Y. Density functional theory study on electronic and photocatalytic properties of orthorhombic AgInS2. *Comput. Mater. Sci.* **2014**, *91*, 159−164.

(55) Saha, S.; Sinha, T.; Mookerjee, A. Electronic structure, chemical bonding, and optical properties of paraelectric BaTiO 3. *Phys. Rev. B* **2000**, *62*, 8828.

(56) Liu, M.; Li, G.; Chen, X. One-pot controlled synthesis of spongelike $CuInS_2$ microspheres for efficient counter electrode with graphene assistance in dye-sensitized solar cells. *ACS Appl. Mater. Interfaces* **2014**, *6*, 2604–2610.

(57) Yuan, Y.-J.; Fang, G.; Chen, D.; Huang, Y.; Yang, L.-X.; Cao, D.-P.; Wang, J.; Yu, Z.-T.; Zou, Z.-G. High light harvesting efficiency $CuInS_2$ quantum dots/TiO_2/MoS_2 photocatalysts for enhanced visible light photocatalytic H 2 production. *Dalton Trans.* **2018**, *47*, 5652–5659.

(58) Hu, J.; Deng, B.; Tang, K.; Wang, C.; Qian, Y. Preparation and phase control of nanocrystalline silver indium sulfides via a hydrothermal route. *J. Mater. Res.* **2001**, *16*, 3411–3415.

(59) Tipcompor, N.; Thongtem, S.; Thongtem, T. Transformation of cubic $AgBiS_2$ from nanoparticles to nanostructured flowers by a microwave-refluxing method. *Ceram. Int.* **2013**, *39*, S383–S387.

(60) Jiang, N.; Wu, R.; Li, J.; Sun, Y.; Jian, J. Ethanol amine-assisted solvothermal growth of wurtzite-structured ZnS thin nanorods. *J. Alloys Compd.* **2012**, *536*, 85–90.

(61) Chen, Z.; Qin, X.; Zhou, T.; Wu, X.; Shao, S.; Xie, M.; Cui, Z. Ethanolamine-assisted synthesis of size-controlled indium tin oxide nanoinks for low temperature solution deposited transparent conductive films. *J. Mater. Chem. C* **2015**, *3*, 11464–11470.

(62) Yao, H.-B.; Gao, M.-R.; Yu, S.-H. Small organic molecule templating synthesis of organic–inorganic hybrid materials: their nanostructures and properties. *Nanoscale* **2010**, *2*, 322–334.

(63) Wang, X.; Zhang, Q.; Wan, Q.; Dai, G.; Zhou, C.; Zou, B. Controllable ZnO architectures by ethanolamine-assisted hydrothermal reaction for enhanced photocatalytic activity. *J. Phys. Chem. C* **2011**, *115*, 2769–2775.

(64) Tian, L.; Vittal, J. J. Synthesis and characterization of ternary $AgInS_2$ nanocrystals by dual-and multiple-source methods. *New J. Chem.* **2007**, 2083–2087.

(65) Sugan, S.; Dhanasekaran, R. In *Synthesis of $AgInS_2$ Semiconductor Nano Crystals by Solvothermal Method*, IOP Conference Series: Materials Science and Engineering; IOP Publishing, 2015; p 012147.

(66) Delgado, G.; Mora, A.; Pineda, C.; Tinoco, T. Simultaneous Rietveld refinement of three phases in the Ag-In-S semiconducting system from X-ray powder diffraction. *MRS Bulletin* **2001**, *36*, 2507–2517.

(67) Borkovska, L.; Romanyuk, A.; Strelchuk, V.; Polishchuk, Y.; Kladko, V.; Raevskaya, A.; Stroyuk, O.; Kryshtab, T. Optical characterization of the $AgInS_2$ nanocrystals synthesized in aqueous media under stoichiometric conditions. *Mater. Sci. Semicond. Process.* **2015**, *37*, 135–142.

(68) Ohrendorf, F.; Haeuseler, H. Lattice dynamics of chalcopyrite type compounds. Part I. Vibrational frequencies. *Cryst. Res. Technol.* **1999**, *34*, 339–349.

(69) Byrne, C.; Fagan, R.; Hinder, S.; McCormack, D. E.; Pillai, S. C. New approach of modifying the anatase to rutile transition temperature in TiO_2 photocatalysts. *RSC Adv.* **2016**, *6*, 95232–95238.

(70) Mathew, S.; Ganguly, P.; Rhatigan, S.; Kumaravel, V.; Byrne, C.; Hinder, S.; Bartlett, J.; Nolan, M.; Pillai, S. Cu-Doped TiO_2: Visible Light Assisted Photocatalytic Antimicrobial Activity. *Appl. Sci.* **2018**, *8*, No. 2067.

(71) Swamy, V.; Kuznetsov, A.; Dubrovinsky, L. S.; Caruso, R. A.; Shchukin, D. G.; Muddle, B. C. Finite-size and pressure effects on the Raman spectrum of nanocrystalline anatase TiO_2. *Phys. Rev. B* **2005**, *71*, No. 184302.

(72) Zhu, Y.; Wang, Y.; Ling, Q.; Zhu, Y. Enhancement of full-spectrum photocatalytic activity over $BiPO_4$/Bi_2WO_6 composites. *Appl. Catal., B* **2017**, *200*, 222–229.

(73) Li, N.; Lv, T.; Yao, Y.; Li, H.; Liu, K.; Chen, T. Compact graphene/MoS_2 composite films for highly flexible and stretchable all-solid-state supercapacitors. *J. Mater. Chem. A* **2017**, *5*, 3267–3273.

(74) Etacheri, V.; Seery, M. K.; Hinder, S. J.; Pillai, S. C. Highly visible light active $TiO_{2-x}N_x$ heterojunction photocatalysts. *Chem. Mater.* **2010**, *22*, 3843–3853.

(75) Leyland, N. S.; Podporska-Carroll, J.; Browne, J.; Hinder, S. J.; Quilty, B.; Pillai, S. C. Highly Efficient F, Cu doped TiO_2 anti-bacterial visible light active photocatalytic coatings to combat hospital-acquired infections. *Sci. Rep.* **2016**, *6*, No. 24770.

(76) Liu, D.; Cai, D.; Yang, Y.; Zhong, H.; Zhao, Y.; Song, Y.; Yang, S.; Wu, H. Solvothermal synthesis of carbon nanotube-$AgBiS_2$ hybrids and their optical limiting properties. *Appl. Surf. Sci.* **2016**, *366*, 30–37.

(77) Sun, M.-H.; Huang, S.-Z.; Chen, L.-H.; Li, Y.; Yang, X.-Y.; Yuan, Z.-Y.; Su, B.-L. Applications of hierarchically structured porous materials from energy storage and conversion, catalysis, photocatalysis, adsorption, separation, and sensing to biomedicine. *Chem. Soc. Rev.* **2016**, *45*, 3479–3563.

(78) Bird, R.; Swift, P. Energy calibration in electron spectroscopy and the re-determination of some reference electron binding energies. *J. Electron Spectrosc. Relat. Phenom.* **1980**, *21*, 227–240.

(79) Ouchene, M.; Senemaud, C.; Belin, E.; Gheorghiu, A.; Theye, M.-L. Influence of disorder on the electronic distribution of InP by X-ray and photoelectron spectroscopies. *J. Non-Cryst. Solids* **1983**, *59*, 625–628.

(80) Vesely, C.; Vesely, C. J.; Langer, D. W. Electronic Core Levels of the II B– VI A Compounds. *Phys. Rev. B* **1971**, *4*, No. 451.

(81) Zhang, Z.; Liu, K.; Feng, Z.; Bao, Y.; Dong, B. Hierarchical sheet-on-sheet $ZnIn_2S_4$/g-C_3N_4 heterostructure with highly efficient photocatalytic H_2 production based on photoinduced interfacial charge transfer. *Sci. Rep.* **2016**, *6*, No. 19221.

(82) Yang, G.; Chen, D.; Ding, H.; Feng, J.; Zhang, J. Z.; Zhu, Y.; Hamid, S.; Bahnemann, D. W. Well-designed 3D $ZnIn_2S_4$ nanosheets/TiO_2 nanobelts as direct Z-scheme photocatalysts for CO_2 photoreduction into renewable hydrocarbon fuel with high efficiency. *Appl. Catal., B* **2017**, *219*, 611–618.

(83) Xia, Y.; Li, Q.; Lv, K.; Tang, D.; Li, M. Superiority of graphene over carbon analogs for enhanced photocatalytic H_2-production activity of $ZnIn_2S_4$. *Appl. Catal., B* **2017**, *206*, 344–352.

(84) Yang, G.; Ding, H.; Chen, D.; Feng, J.; Hao, Q.; Zhu, Y. Construction of urchin-like $ZnIn_2S_4$-Au-TiO_2 heterostructure with enhanced activity for photocatalytic hydrogen evolution. *Appl. Catal., B* **2018**, *234*, 260–267.

(85) Han, C.; Luque, R.; Dionysiou, D. D. Facile preparation of controllable size monodisperse anatase titania nanoparticles. *Chem. Commun.* **2012**, *48*, 1860–1862.

(86) Tian, L.; Vittal, J. J. Synthesis and characterization of ternary $AgInS_2$ nanocrystals by dual-and multiple-source methods. *New J. Chem.* **2007**, *31*, 2083–2087.

(87) Panneri, S.; Ganguly, P.; Nair, B. N.; Mohamed, A. A. P.; Warrier, K. G. K.; Hareesh, U. N. S. Role of precursors on the photophysical properties of carbon nitride and its application for antibiotic degradation. *Environ. Sci. Pollut. Res.* **2017**, *24*, 8609–8618.

(88) Zhang, M.; Li, X.; Zhao, Q.; Fan, S.; Jiang, Z.; Chen, G. AgInS 2 nanoparticles modified TiO_2 nanotube array electrodes: Ultrasonic-assisted SILAR preparation and mechanism of enhanced photo-electrocatalytic activity. *Mol. Catal.* **2017**, *442*, 97–106.

(89) He, W.; Jia, H.; Yang, D.; Xiao, P.; Fan, X.; Zheng, Z.; Kim, H.-K.; Wamer, W. G.; Yin, J.-J. Composition directed generation of reactive oxygen species in irradiated mixed metal sulfides correlated with their photocatalytic activities. *ACS Appl. Mater. Interfaces* **2015**, *7*, 16440–16449.

(90) Nosaka, Y.; Nosaka, A. Y. Generation and detection of reactive oxygen species in photocatalysis. *Chem. Rev.* **2017**, *117*, 11302–11336.

(91) Barbieriková, Z.; Plížingrová, E.; Motlochová, M.; Bezdička, P.; Boháček, J.; Dvoranová, D.; Mazúr, M.; Kupčík, J.; Jirkovský, J.; Šubrt, J. N-doped titanium dioxide nanosheets: Preparation, characterization and UV/visible-light activity. *Appl. Catal., B* **2018**, *232*, 397–408.

(92) Zhu, X.-D.; Wang, Y.-J.; Sun, R.-J.; Zhou, D.-M. Photocatalytic degradation of tetracycline in aqueous solution by nanosized TiO_2. *Chemosphere* **2013**, *92*, 925–932.

(93) Borghi, A. A.; Palma, M. S. A. Tetracycline: production, waste treatment and environmental impact assessment. *Braz. J. Pharm. Sci.* **2014**, *50*, 25–40.

(94) Bolobajev, J.; Trapido, M.; Goi, A. Effect of iron ion on doxycycline photocatalytic and Fenton-based autocatalytic decomposition. *Chemosphere* **2016**, *153*, 220−226.

(95) Gordienko, A.; Filippov, D. Electronic Structure of OR-AgInS$_2$ and TiO$_2$ Crystals and Its Differential Characteristics. *Phys. Solid State* **2018**, *60*, 858−864.

(96) Deng, F.; Zhong, F.; Lin, D.; Zhao, L.; Liu, Y.; Huang, J.; Luo, X.; Luo, S.; Dionysiou, D. D. One-step hydrothermal fabrication of visible-light-responsive AgInS$_2$/SnIn$_4$S$_8$ heterojunction for highly-efficient photocatalytic treatment of organic pollutants and real pharmaceutical industry wastewater. *Appl. Catal., B* **2017**, *219*, 163−172.